Direct Measurement of the Nickel Spectrum in Cosmic Rays in the Energy Range from 8.8 GeV/n to 240 GeV/n with CALET on the International Space Station

O. Adriani,[1,2] Y. Akaike,[3,4,*] K. Asano,[5] Y. Asaoka,[5] E. Berti,[1,2] G. Bigongiari,[6,7,†] W. R. Binns,[8] M. Bongi,[1,2] P. Brogi,[6,7] A. Bruno,[9] J. H. Buckley,[8] N. Cannady,[10,11,12] G. Castellini,[13] C. Checchia,[6,7,‡] M. L. Cherry,[14] G. Collazuol,[15,16] K. Ebisawa,[17] A. W. Ficklin,[14] H. Fuke,[17] S. Gonzi,[1,2] T. G. Guzik,[14] T. Hams,[10] K. Hibino,[18] M. Ichimura,[19] K. Ioka,[20] W. Ishizaki,[5] M. H. Israel,[8] K. Kasahara,[21] J. Kataoka,[22] R. Kataoka,[23] Y. Katayose,[24] C. Kato,[25] N. Kawanaka,[20,26] Y. Kawakubo,[14] K. Kobayashi,[3,4] K. Kohri,[27] H. S. Krawczynski,[8] J. F. Krizmanic,[11] P. Maestro,[6,7] P. S. Marrocchesi,[6,7] A. M. Messineo,[28,7] J. W. Mitchell,[11] S. Miyake,[29] A. A. Moiseev,[30,11,12] M. Mori,[31] N. Mori,[2] H. M. Motz,[32] K. Munakata,[25] S. Nakahira,[17] J. Nishimura,[17] G. A. de Nolfo,[9] S. Okuno,[18] J. F. Ormes,[33] N. Ospina,[15,16] S. Ozawa,[34] L. Pacini,[1,13,2] P. Papini,[2] B. F. Rauch,[8] S. B. Ricciarini,[13,2] K. Sakai,[10,11,12] T. Sakamoto,[35] M. Sasaki,[30,11,12] Y. Shimizu,[18] A. Shiomi,[36] P. Spillantini,[1] F. Stolzi,[6,7,§] S. Sugita,[35] A. Sulaj,[6,7] M. Takita,[5] T. Tamura,[18] T. Terasawa,[5] S. Torii,[3] Y. Tsunesada,[37,38] Y. Uchihori,[39] E. Vannuccini,[2] J. P. Wefel,[14] K. Yamaoka,[40] S. Yanagita,[41] A. Yoshida,[35] K. Yoshida,[21] and W. V. Zober[8]

(CALET Collaboration)

[1]*Department of Physics, University of Florence, Via Sansone, 1 - 50019 Sesto Fiorentino, Italy*
[2]*INFN Sezione di Florence, Via Sansone, 1 - 50019 Sesto Fiorentino, Italy*
[3]*Waseda Research Institute for Science and Engineering, Waseda University, 17 Kikuicho, Shinjuku, Tokyo 162-0044, Japan*
[4]*JEM Utilization Center, Human Spaceflight Technology Directorate,*
Japan Aerospace Exploration Agency, 2-1-1 Sengen, Tsukuba, Ibaraki 305-8505, Japan
[5]*Institute for Cosmic Ray Research, The University of Tokyo, 5-1-5 Kashiwa-no-Ha, Kashiwa, Chiba 277-8582, Japan*
[6]*Department of Physical Sciences, Earth and Environment, University of Siena, via Roma 56, 53100 Siena, Italy*
[7]*INFN Sezione di Pisa, Polo Fibonacci, Largo B. Pontecorvo, 3 - 56127 Pisa, Italy*
[8]*Department of Physics and McDonnell Center for the Space Sciences, Washington University,*
One Brookings Drive, St. Louis, Missouri 63130-4899, USA
[9]*Heliospheric Physics Laboratory, NASA/GSFC, Greenbelt, Maryland 20771, USA*
[10]*Center for Space Sciences and Technology, University of Maryland,*
Baltimore County, 1000 Hilltop Circle, Baltimore, Maryland 21250, USA
[11]*Astroparticle Physics Laboratory, NASA/GSFC, Greenbelt, Maryland 20771, USA*
[12]*Center for Research and Exploration in Space Sciences and Technology, NASA/GSFC, Greenbelt, Maryland 20771, USA*
[13]*Institute of Applied Physics (IFAC), National Research Council (CNR), Via Madonna del Piano, 10, 50019 Sesto Fiorentino, Italy*
[14]*Department of Physics and Astronomy, Louisiana State University, 202 Nicholson Hall, Baton Rouge, Louisiana 70803, USA*
[15]*Department of Physics and Astronomy, University of Padova, Via Marzolo, 8, 35131 Padova, Italy*
[16]*INFN Sezione di Padova, Via Marzolo, 8, 35131 Padova, Italy*
[17]*Institute of Space and Astronautical Science, Japan Aerospace Exploration Agency,*
3-1-1 Yoshinodai, Chuo, Sagamihara, Kanagawa 252-5210, Japan
[18]*Kanagawa University, 3-27-1 Rokkakubashi, Kanagawa, Yokohama, Kanagawa 221-8686, Japan*
[19]*Faculty of Science and Technology, Graduate School of Science and Technology, Hirosaki University,*
3, Bunkyo, Hirosaki, Aomori 036-8561, Japan
[20]*Yukawa Institute for Theoretical Physics, Kyoto University, Kitashirakawa Oiwake-cho, Sakyo-ku, Kyoto 606-8502, Japan*
[21]*Department of Electronic Information Systems, Shibaura Institute of Technology, 307 Fukasaku, Minuma, Saitama 337-8570, Japan*
[22]*School of Advanced Science and Engineering, Waseda University, 3-4-1 Okubo, Shinjuku, Tokyo 169-8555, Japan*
[23]*National Institute of Polar Research, 10-3, Midori-cho, Tachikawa, Tokyo 190-8518, Japan*
[24]*Faculty of Engineering, Division of Intelligent Systems Engineering, Yokohama National University,*
79-5 Tokiwadai, Hodogaya, Yokohama 240-8501, Japan
[25]*Faculty of Science, Shinshu University, 3-1-1 Asahi, Matsumoto, Nagano 390-8621, Japan*
[26]*Department of Astronomy, Graduate School of Science, Kyoto University,*
Kitashirakawa Oiwake-cho, Sakyo-ku, Kyoto 606-8502, Japan
[27]*Institute of Particle and Nuclear Studies, High Energy Accelerator Research Organization,*
1-1 Oho, Tsukuba, Ibaraki 305-0801, Japan
[28]*University of Pisa, Polo Fibonacci, Largo B. Pontecorvo, 3 - 56127 Pisa, Italy*
[29]*Department of Electrical and Electronic Systems Engineering, National Institute of Technology,*
Ibaraki College, 866 Nakane, Hitachinaka, Ibaraki 312-8508, Japan
[30]*Department of Astronomy, University of Maryland, College Park, Maryland 20742, USA*
[31]*Department of Physical Sciences, College of Science and Engineering, Ritsumeikan University, Shiga 525-8577, Japan*

^{32}*Faculty of Science and Engineering, Global Center for Science and Engineering, Waseda University,*
3-4-1 Okubo, Shinjuku, Tokyo 169-8555, Japan
^{33}*Department of Physics and Astronomy, University of Denver, Physics Building,*
Room 211, 2112 East Wesley Avenue, Denver, Colorado 80208-6900, USA
^{34}*Quantum ICT Advanced Development Center, National Institute of Information and Communications Technology,*
4-2-1 Nukui-Kitamachi, Koganei, Tokyo 184-8795, Japan
^{35}*College of Science and Engineering, Department of Physics and Mathematics, Aoyama Gakuin University,*
5-10-1 Fuchinobe, Chuo, Sagamihara, Kanagawa 252-5258, Japan
^{36}*College of Industrial Technology, Nihon University, 1-2-1 Izumi, Narashino, Chiba 275-8575, Japan*
^{37}*Division of Mathematics and Physics, Graduate School of Science, Osaka City University,*
3-3-138 Sugimoto, Sumiyoshi, Osaka 558-8585, Japan
^{38}*Nambu Yoichiro Institute of Theoretical and Experimental Physics, Osaka City University,*
3-3-138 Sugimoto, Sumiyoshi, Osaka 558-8585, Japan
^{39}*National Institutes for Quantum and Radiation Science and Technology, 4-9-1 Anagawa, Inage, Chiba 263-8555, Japan*
^{40}*Nagoya University, Furo, Chikusa, Nagoya 464-8601, Japan*
^{41}*College of Science, Ibaraki University, 2-1-1 Bunkyo, Mito, Ibaraki 310-8512, Japan*

The relative abundance of cosmic ray nickel nuclei with respect to iron is by far larger than for all other transiron elements; therefore it provides a favorable opportunity for a low background measurement of its spectrum. Since nickel, as well as iron, is one of the most stable nuclei, the nickel energy spectrum and its relative abundance with respect to iron provide important information to estimate the abundances at the cosmic ray source and to model the Galactic propagation of heavy nuclei. However, only a few direct measurements of cosmic-ray nickel at energy larger than ~ 3 GeV/n are available at present in the literature, and they are affected by strong limitations in both energy reach and statistics. In this Letter, we present a measurement of the differential energy spectrum of nickel in the energy range from 8.8 to 240 GeV/n, carried out with unprecedented precision by the Calorimetric Electron Telescope (CALET) in operation on the International Space Station since 2015. The CALET instrument can identify individual nuclear species via a measurement of their electric charge with a dynamic range extending far beyond iron (up to atomic number $Z = 40$). The particle's energy is measured by a homogeneous calorimeter (1.2 proton interaction lengths, 27 radiation lengths) preceded by a thin imaging section (3 radiation lengths) providing tracking and energy sampling. This Letter follows our previous measurement of the iron spectrum [O. Adriani *et al.* (CALET Collaboration), Phys. Rev. Lett. **126**, 241101 (2021).], and it extends our investigation on the energy dependence of the spectral index of heavy elements. It reports the analysis of nickel data collected from November 2015 to May 2021 and a detailed assessment of the systematic uncertainties. In the region from 20 to 240 GeV/n our present data are compatible within the errors with a single power law with spectral index -2.51 ± 0.07.

Introduction.—The energy spectra and relative abundances of cosmic rays (CR) are key observables for a theoretical understanding of the acceleration and propagation mechanisms of charged particles in our Galaxy [1–15]. Direct measurements by space-borne instruments have recently achieved a level of unprecedented precision, thanks to long term observations and their capability to identify individual chemical elements. Direct measurements from high-altitude balloons and indirect measurements from ground based arrays convey important complementary information, albeit

with different systematic uncertainties. The extensions to higher energies of CR spectral data have shown unexpected deviations from a single power law, as in the case of the recently observed double broken spectral shape of the proton spectrum in the multi-TeV domain, reported by the DAMPE [16] and Calorimetric Electron Telescope (CALET) [17] experiment. A progressive spectral hardening (as a function of energy) has been established for light elements and heavier nuclei [18–22] with an onset at a few hundred GeV/n. Also, a spectral softening has been observed in the TeV domain for proton and helium as reported by the DAMPE [16,23], CALET [17], and NUCLEON [24] experiments. The spectral study of heavy elements was recently extended to higher energies with the publication of the iron spectrum by the AMS-02 [25] and CALET [26] experiments.

In this Letter, we pursue the study of elements sitting on the high side of the periodic table, where nickel—with

much larger abundance than all other transiron elements—provides a favorable opportunity for a low background measurement of its spectrum.

Space-borne direct measurements of CR nickel nuclei include the spectrum measured from 0.6 to 35 GeV/n by the French-Danish C2 instrument HEAO3-C2 [27] onboard the NASA HEAO3 satellite (launched in 1979) and the recent measurement by the NUCLEON experiment (launched in 2014) [28] in the energy range $\sim$51–511 GeV/n. Measurements in the lower energy range 50–550 MeV/n were carried out, during the 2009–2010 solar minimum period, by Cosmic Ray Isotope Spectrometer (CRIS) [29] onboard the Advanced Composition Explorer at the L1 Lagrange point. Data up to $\sim$500 MeV/n [30] were collected by the *Voyager 1* spacecraft after the start of observations of the local interstellar energy spectra of Galactic cosmic-ray nuclei (August 2012).

Earlier measurements with balloon experiments have a limited statistics and energy reach. They include (i) the High Energy Nuclei (HEN) telescope [31] at nickel energies up to about 10.5 GeV/n (3 flights in 1971 and 1972 for a total of 7.6 m^2 sr hrs); (ii) the scintillation-Cherenkov telescope (hereafter cited as Balloon 1975) [32] from 1 to 10 GeV/n (2 flights in 1975 with a total exposure of 20 m^2 sr hrs); (iii) the multielement Cherenkov telescope [33] from 0.3–50 GeV/n (3 flights in 1974 and one in 1976); (iv) the Cosmic Ray Isotope Instrument System (CRISIS) [34] from 600–900 MeV/n ($\sim$57 h afloat in 1975); (v) the Large Isotopic Composition Experiment (ALICE) [35] at energies near 1 GeV/n (flown for 14.7 hrs in 1987).

In this Letter we present a measurement of the differential energy spectrum of CR nickel in the energy range from 8.8 to 240 GeV/n carried out, with unprecedented precision, with CALET onboard the International Space Station (ISS). Though optimized for the measurement of the all-electron spectrum [36,37], CALET has an excellent charge identification capability to tag individual CR elements [38–41] from proton to nickel nuclei (and above). It can explore particle energies up to the PeV scale thanks to its large dynamic range, adequate calorimetric depth, and accurate tracking. CALET published accurate spectral measurements of electrons [37], protons [38], carbon [22], oxygen [22], and iron [26]. Preliminary updates of proton, helium, boron, and boron to carbon ratio analyses were presented at the ICRC-2021 conference [42].

CALET instrument.—Charge identification is carried out by the charge detector (CHD), a two-layered hodoscope of plastic scintillator paddles. It can resolve individual elements from atomic number $Z = 1$ to $Z = 40$ with excellent charge resolution spanning from 0.15 charge units for C to 0.35 charge units for Fe [43]. The particle's energy is measured with the total absorption calorimeter (TASC), a lead-tungstate homogeneous calorimeter [27 radiation lengths (r.l.), 1.2 proton interaction lengths] preceded by

a thin (3 r.l.) preshower imaging calorimeter (IMC). The latter is equipped with 16 layers of thin scintillating fibers (1 mm^2 square cross section) read out individually and interleaved with tungsten absorbers. The IMC provides tracking capabilities as well as an independent charge measurement, via multiple samples of specific energy loss (dE/dx) in each fiber, up to the onset of saturation which occurs for ions above silicon. Therefore charge identification for nickel and neighboring elements relies on CHD only. More details on the instrument and on the trigger system can be found in the Supplemental Material of Ref. [36]. CALET was launched on August 19, 2015, and installed on the Japanese experiment module exposed facility of the ISS. The on-orbit commissioning phase was successfully completed in the first days of October 2015. Calibration and test of the instrument took place at the CERN-SPS during five campaigns between 2010 and 2015 with beams of electrons, protons, and relativistic ions [44–46].

Data analysis.—The flight data (FD) used in the present analysis were collected over a period of 2038 days of CALET operation. The total observation live time for the high-energy (HE) shower trigger [47] is $T \sim 4.1 \times 10^4$ hours, corresponding to 86.0% of total observation time.

Individual on-orbit calibration of all channels is performed with a dedicated trigger mode [46,47] allowing the selection of penetrating protons and He particles. First, raw data are corrected for gain differences among the channels, light output nonuniformity, and any residual dependence on time and temperature. After calibration, a single "best track" is reconstructed for each event with an associated estimate of its charge and energy.

The particle's direction and entrance point are reconstructed from the coordinates of the scintillating fibers in the IMC. The tracking algorithm, based on a combinatorial Kalman filter, identifies the incident track in the presence of background hits generated by backscattered radiation from the TASC [48]. The angular resolution and the spatial resolution for the impact point on the CHD are $\sim$0.08° and $\sim$180 μm respectively.

Physics processes and interactions in the apparatus are simulated via Monte Carlo (MC) techniques, based on the EPICS package [49,50] which implements the hadronic interaction model DPMJET-III [51]. The instrument configuration and detector response are detailed in the simulation code which provides digitized signals from all channels. An independent analysis based on GEANT4 [52] is also performed to assess the systematic uncertainties. In this analysis, only the ^{58}Ni isotope was considered since its mass difference with respect to other isotopes (mainly ^{60}Ni) is less than 3%.

Charge measurement.—The particle's charge Z is reconstructed from the signals of the CHD paddles traversed by the incident particle and properly corrected for its path length. Either CHD layer provides an independent dE/dx

measurement which has to be corrected for the quenching effect in the scintillator's light yield. The latter is parametrized by fitting selected FD samples of each nuclear species to a "halo" model [43] as a function of Z^2. The resulting curves are then used to reconstruct a charge value in either layer (Z_{CHDX}, Z_{CHDY}) on an event-by-event basis [22]. The presence of an increasing amount of backscatters from the TASC at higher energy generates additional energy deposits in the CHD that add on to the primary particle ionization signal and may induce a wrong charge identification. This effect causes a systematic displacement of the CHDX/CHDY charge peaks to higher values (up to 0.8 charge units) with respect to the nominal charge position. Therefore it is necessary to restore the nickel peak position to its nominal value, $Z = 28$, by an energy dependent charge correction applied separately to the FD and the MC data. A similar correction is applied to iron and nearby elements. The CHD charge resolution σ_Z, obtained by combining the average of the Z_{CHDX} and Z_{CHDY} signal is 0.39 in charge units, and it is shown in Fig. S1 of the Supplemental Material [53]. Background contamination from neighbor elements misidentified as nickel is shown in Fig. S2 of the Supplemental Material [53]. Between 100 GeV and 1 TeV it is mainly due to iron and secondly to cobalt. Above 1 TeV the iron contribution is the most important. Contamination from heavier nuclei is negligible.

Energy measurement.—For each event, the shower energy E_{TASC} is calculated as the sum of the energy deposits of all TASC logs, after merging the calibrated gain ranges of each channel [47]. The energy response derived from the MC simulations was tuned using the results of a beam test carried out at the CERN-SPS in 2015 [44] with beams of accelerated ion fragments of 13, 19, and 150 GeV/c/n momentum per nucleon (as described in the Supplemental Material of Ref. [22]). Correction factors are 6.7% for $E_{TASC} < 45$ GeV and 3.5% for $E_{TASC} > 350$ GeV, respectively. A linear interpolation is used to determine the correction factor for intermediate energies.

Event selection.—The onboard HE shower trigger, based on the coincidence of the summed dynode signals of the last four IMC layers and the top TASC layer (TASCX1) is fully efficient for elements heavier than oxygen. Therefore, an offline trigger confirmation, as required for the analysis of lower charge elements [22,38], is not necessary for nickel, because the HE trigger threshold is far below the signal amplitude expected from a nickel ion at minimum ionization (MI) and the trigger efficiency is close to 100%. However, in order to select interacting particles, a deposit larger than 2 standard deviations of the MI peak is required in at least one of the first four layers of the TASC.

Events with one well-fitted track crossing the whole detector from the top of the CHD to the TASC bottom layer (and clear from the edges of TASCX1 by at least 2 cm) are selected. The fiducial geometrical factor for this category of events is $S\Omega \sim 510$ cm^2 sr, corresponding to about 50% of the CALET total acceptance.

Particles undergoing a charge-changing nuclear interaction in the upper part of the instrument are removed by requiring that the difference between the charges from either layer of the CHD be less than 1.5 charge units. The cross plot of the Z_{CHDY} vs Z_{CHDX} charge, in Fig. 1, shows the nickel events selection: candidates are contained within an ellipse centered at $Z = 28$ with $1.4\sigma_x$ and $1.4\sigma_y$ wide semimajor and minor axes (with both variances depending on the energy) for Z_{CHDX} and Z_{CHDY}, respectively, and rotated clockwise by 45°. Event selections are identical for the MC and the FD.

Energy unfolding.—As detailed in Ref. [26] for iron, the TASC crystals are subject to a light quenching phenomenon which is not reproduced by the MC simulations. Therefore a quenching correction is extracted from the FD and applied *a posteriori* to the MC energy deposits generated by noninteracting primary particles in the TASC logs. Distributions of E_{TASC} for Ni selected candidates are shown in Fig. S2 of the Supplemental Material [53], with a sample of 5.2×10^3 events.

In order to take into account the limited calorimetric energy resolution for hadrons (of the order of ~30%) an energy unfolding algorithm is applied to correct for bin-to-bin migration effects. In this analysis, we used the Bayesian approach [54] implemented within the RooUnfold package [55] of the ROOT analysis framework [56]. Each element of the response matrix represents the probability that a primary
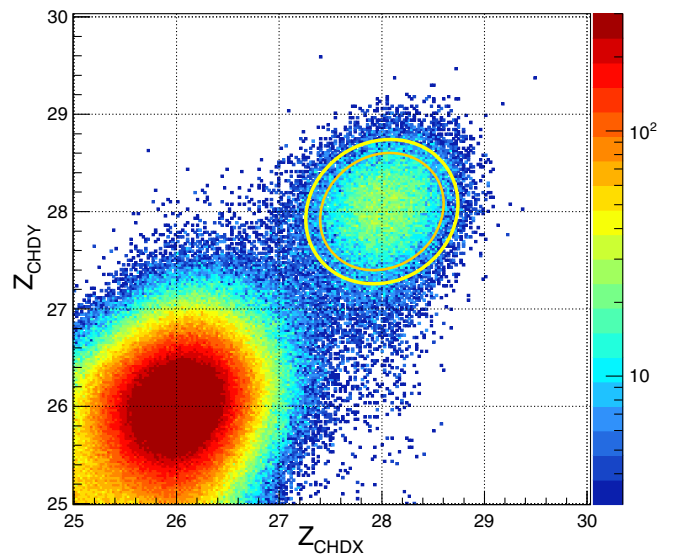

FIG. 1. Crossplot of Z_{CHDY} vs Z_{CHDX} reconstructed charges in the elemental range between Mn ($Z = 25$) and Zn ($Z = 30$) before removing charge-changing nuclear interactions. Nickel candidates are selected inside an ellipse with semiminor and major axes $1.4\sigma_x$ and $1.4\sigma_y$, respectively, rotated clockwise by 45°. The maximum and the minimum elliptical selection (depending on the energy) are indicated by the yellow and the orange ellipses in the figure.

nucleus in a given energy interval of the CR spectrum produces an energy deposit falling into a given bin of E_{TASC}. The response matrix is derived using the MC simulation after applying the same selection procedure as for flight data, and it is shown in Fig. S6 of the Supplemental Material [53].

Differential energy spectrum.—The energy spectrum is obtained from the unfolded energy distribution as follows:

$$\Phi(E) = \frac{N(E)}{\Delta E \varepsilon(E) S \Omega T} \qquad (1)$$

$$N(E) = U[N_{\text{obs}}(E_{\text{TASC}}) - N_{\text{bg}}(E_{\text{TASC}})] \qquad (2)$$

where $S\Omega$ and T are the geometrical factor and the live time respectively, ΔE denotes the energy bin width, E is the geometric mean of the lower and upper bounds of the bin [57], $N(E)$ is the bin content in the unfolded distribution, $\varepsilon(E)$ is the total selection efficiency (Fig. S3 of the Supplemental Material [53]), $U()$ is the unfolding procedure operator, $N_{\text{obs}}(E_{\text{TASC}})$ is the bin content of observed energy distribution (including background), and $N_{\text{bg}}(E_{\text{TASC}})$ is the bin content of background events in the observed energy distribution. In the energy range between 10^2 and 10^3 GeV of E_{TASC} the background fraction is $N_{\text{bg}}/N_{\text{obs}} \sim 1\%$. Starting from 10^3 GeV it increases up to 10% at 10^4 GeV.

Systematic uncertainties.—The most important sources of systematics uncertainties in the nickel analysis are due to the MC model and event selection at high energy. The systematic error related to charge identification was studied by varying the semiminor and major axes of the elliptical selection up to $\pm 15\%$ corresponding to a variation of charge selection efficiency of $\pm 17\%$. The result was an (energy bin dependent) flux variation lower than 4% below $100 \text{ GeV}/n$ and increasing to $\sim 8\%$ at $200 \text{ GeV}/n$. A comparison between different MC algorithms is in order as it is not possible to validate the MC simulations with beam test data at high energy. A comparative study of key distributions was carried out with EPICS and GEANT4 showing that the respective total selection efficiencies for Ni are in agreement within $\sim 3\%$ over the whole energy range (Fig. S3 of the Supplemental Material [53]). The difference between the two energy response matrices is contained between -5% and $+5\%$. The resulting fluxes show a difference around $\sim 5\%$ below $40 \text{ GeV}/n$ and less than $\sim 10\%$ in the $100 - 200 \text{ GeV}/n$ region.

The uncertainty on the energy scale correction is $\pm 2\%$ and depends on the accuracy of the beam test calibration. It causes a rigid shift of the flux ($\pm 4\%$) above $30 \text{ GeV}/n$, not affecting the spectral shape. As the beam test model was not identical to the instrument in flight [38], the difference in the spectrum ($\pm 5\%$ up to $140 \text{ GeV}/n$) obtained with either configuration was modeled and included in the systematic error.

The uncertainties due to the unfolding procedure were evaluated with different response matrices computed by varying the spectral index (between -2.9 and -2.2) of the MC generation spectrum.

As the trigger threshold is much smaller than the energy of a noninteracting nickel nucleus, the HE trigger efficiency is close to 100% in the whole energy range with a negligible contribution to the systematic error. The fraction of interactions (Fig. S5 of the Supplemental Material [53]) in the CHD, and above it, was checked by comparing the MC and the FD as explained in the Supplemental Material. The contribution due to a shower event cut, rejecting noninteracting particles (4% around 10 GeV and 2% above), was evaluated and included in the systematic uncertainties.

Possible inaccuracy of track reconstruction could affect the determination of the geometrical acceptance. The contamination due to off-acceptance events that are erroneously reconstructed inside the fiducial acceptance was estimated by MC to be $\sim 1\%$ at $10 \text{ GeV}/n$ while decreasing to less than 0.1% above $60 \text{ GeV}/n$. The systematic uncertainty on the tracking efficiency is negligible [22]. A different tracking procedure, described in Ref. [58], was also used to study possible systematic uncertainties in tracking efficiency. The result is consistent with the Kalman filter algorithm. The systematic error related to background contamination is assessed by varying the contamination level by as much as $\pm 50\%$. The result was a flux variation around 1% below $100 \text{ GeV}/n$, increasing to 3% at $200 \text{ GeV}/n$.

The systematic error related to the atomic mass of nickel isotope composition reduces the normalization by 2.2%. Additional energy-independent systematic uncertainties
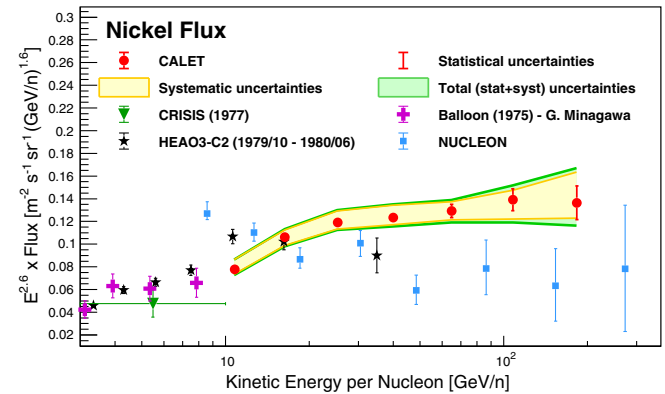

FIG. 2. CALET nickel flux (multiplied by $E^{2.6}$) as a function of kinetic energy per nucleon. Error bars of the CALET data (red) represent the statistical uncertainty only, the yellow band indicates the quadrature sum of systematic errors, while the green band indicates the quadrature sum of statistical and systematic errors. Also plotted are the measurements from Balloon 1975 [32], CRISIS [34], HEAO3-C2 [27], and NUCLEON [28]. This figure is reproduced and enlarged in Fig. S9 of the Supplemental Material [53].
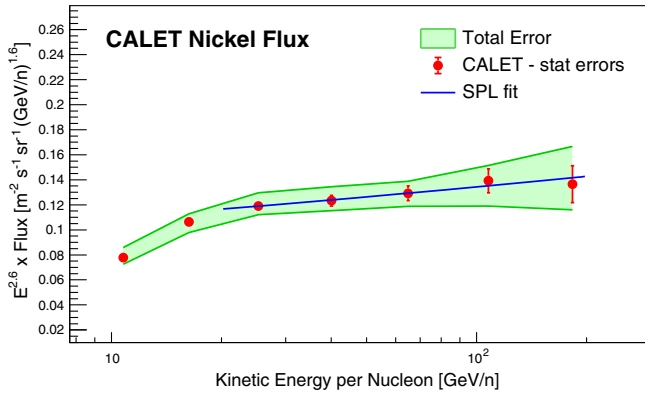
FIG. 3. Fit of the CALET nickel energy spectrum to an SPL function (blue line) in the energy range $[20, 240]$ GeV/n. The flux is multiplied by $E^{2.6}$ where E is the kinetic energy per nucleon. The error bars are representative of purely statistical errors.
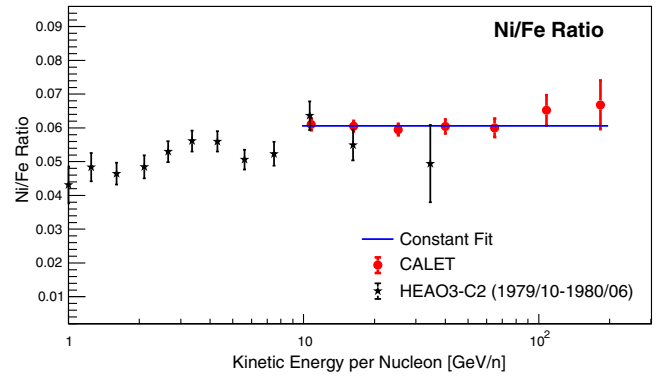

FIG. 4. Nickel to iron flux ratio measured with CALET (red points). The errors bars are representative of statistical errors only. Data are fitted with a constant function giving Ni/Fi $= 0.061 \pm 0.001$. Also plotted is the result from HEAO3-C2 [27].

affecting the flux normalization include live time (3.4%), long-term stability ($< 2.7\%$), and geometrical factor ($\sim 1.6\%$), as detailed in the Supplemental Material of Ref. [36]. The energy dependence of all systematic errors for nickel analysis is shown in Fig. S8 of the Supplemental Material [53]. The total systematic error is computed as the sum in quadrature of all the sources of systematics in each energy bin.

Results.—The nickel differential spectrum in kinetic energy per nucleon measured by CALET in the energy range from 8.8 to 240 GeV/n is shown in Fig. 2, where current uncertainties including statistical and systematic errors are bounded within a green band. The CALET spectrum is compared with the results from Balloon 1975 [32], CRISIS [34], HEAO3-C2 [27], and NUCLEON [28]. The nickel flux measurements with CALET are tabulated in Table I of the Supplemental Material [53] where statistical and systematic errors are also shown. CALET and HEAO3-C2 nickel spectra have similar flux normalization in the common interval of energies. CALET and NUCLEON differ in the shape although the two measurements show a similar flux normalization at low energy.

Figure 3 shows a fit to the CALET nickel flux with a single power law function (SPL)

$$\Phi(E) = C\left(\frac{E}{1 \text{ GeV}/n}\right)^{\gamma} \qquad (3)$$

where γ is the spectral index and C is the normalization factor.

The fit is performed from 20 to 240 GeV/n and gives $\gamma = -2.51 \pm 0.04(\text{stat}) \pm 0.06(\text{sys})$ with a $\chi^2/\text{d.o.f.} = 0.3/3$. Below 20 GeV/$n$ the observed Ni flux softening is similar to the one found for iron and lighter primaries. To better understand the nickel spectral behavior we report also the nickel to iron ratio as a function of kinetic energy

per nucleon (see Fig. 4). Our measure extends the results of previous experiments (i.e., HEAO3-C2) up to 240 GeV/n. The fit, performed from 8.8 to 240 GeV/n, gives a constant value of $0.061 \pm 0.001(\text{stat})$ with the $\chi^2/\text{d.o.f.} = 2.3/6$.

The experimental limitations of the present measurement (i.e., low statistics as well as large systematic errors for the highest energy bins) do not yet allow one to test the hypothesis of a spectral shape different from a single power law in the region above 20 GeV/n. As a matter of fact, current expectations (e.g., [5,8]) for a detectable spectral hardening of nickel are still under debate.

Conclusion.—In this paper, based on 67 months of observations with CALET on the ISS, we report for the first time a measurement of the energy spectrum of nickel over an extended energy range up to 240 GeV/n and with a significantly better precision than most of the existing measurements. The nickel spectrum behavior below 20 GeV/n is similar to the one observed for iron and lighter primaries. Above 20 GeV/n, our present observations are consistent with the hypothesis of an SPL spectrum up to 240 GeV/n. Beyond this limit, the uncertainties given by our present statistics and large systematics do not allow us to draw a significant conclusion on a possible deviation from a single power law. A SPL fit in this region yields a spectral index value $\gamma = -2.51 \pm 0.07$. The flat behavior of the nickel to iron ratio suggests that the spectral shapes of Fe and Ni are the same within the experimental accuracy. This suggests a similar acceleration and propagation behavior as expected from the small difference in atomic number and weight between Fe and Ni nuclei. An extended dataset, as expected beyond the 67 month period of continuous observations accomplished so far, will not only improve the most important statistical limitations of the present measurement, but also our understanding of the instrument response in view of a further reduction of systematic uncertainties.

---

[*]Corresponding author.
yakaike@aoni.waseda.jp
[†]Corresponding author.
bigongiari2@unisi.it
[‡]Corresponding author.
caterina.checchia2@unisi.it
[§]Corresponding author.
francesco.stolzi@unisi.it

[1] L. O. Drury, Mon. Not. R. Astron. Soc. **415**, 1807 (2011).
[2] Y. Ohira and K. Ioka, Astrophys. J. Lett. **729**, L13 (2011).
[3] M. A. Malkov, P. H. Diamond, and R. Z. Sagdeev, Phys. Rev. Lett. **108**, 081104 (2012).
[4] P. Blasi, E. Amato, and P. D. Serpico, Phys. Rev. Lett. **109**, 061101 (2012).
[5] N. Tomassetti, Astrophys. J. Lett. **752**, L13 (2012).
[6] A. Vladimirov, G. Johannesson, I. Moskalenko, and T. Porter, Astrophys. J. **752**, 68 (2012).
[7] V. Ptuskin, V. Zirakashvili, and E. S. Seo, Astrophys. J. **763**, 47 (2013).
[8] S. Thoudam and J. R. Hörandel, Astron. Astrophys. **567**, A33 (2014).
[9] G. Bernard, T. Delahaye, Y.-Y. Keum, W. Liu, P. Salati, and R. Taillet, Astron. Astrophys. **555**, A48 (2013).
[10] P. D. Serpico, Proc. Sci., ICRC2015 (**2015**) 009.
[11] Y. Ohira, N. Kawanaka, and K. Ioka, Phys. Rev. D **93**, 083001 (2016).
[12] C. Evoli, P. Blasi, G. Morlino, and R. Aloisio, Phys. Rev. Lett. **121**, 021102 (2018).
[13] C. Evoli, R. Aloisio, and P. Blasi, Phys. Rev. D **99**, 103023 (2019).
[14] D. Caprioli et al., Proc. Sci., ICRC2021 (**2021**) 482.
[15] P. Lipari, Proc. Sci., ICRC2021 (**2021**) 169.
[16] Q. An et al. (DAMPE Collaboration), Sci. Adv. **5**, eaax3793 (2019).
[17] K. Kobayashi and P. S. Marrocchesi, Proc. Sci., ICRC2021 (**2021**) 098.
[18] M. Aguilar et al. (AMS Collaboration), Phys. Rev. Lett. **119**, 251101 (2017).
[19] M. Aguilar et al. (AMS Collaboration), Phys. Rev. Lett. **120**, 021101 (2018).
[20] M. Aguilar et al. (AMS Collaboration), Phys. Rev. Lett. **124**, 211102 (2020).
[21] H. S. Ahn et al. (CREAM Collaboration), Astrophys. J. Lett. **714**, L89 (2010).
[22] O. Adriani et al. (CALET Collaboration), Phys. Rev. Lett. **125**, 251102 (2020).
[23] F. Alemanno et al. (DAMPE Collaboration), Phys. Rev. Lett. **126**, 201102 (2021).
[24] V. Grebenyuk et al. (NUCLEON Collaboration), Adv. Space Res. **64**, 2546 (2019).
[25] M. Aguilar et al. (AMS Collaboration), Phys. Rev. Lett. **126**, 041104 (2021).
[26] O. Adriani et al. (CALET Collaboration), Phys. Rev. Lett. **126**, 241101 (2021).
[27] J. J. Engelmann et al. (HEAO3-C2 Collaboration), Astron. Astrophys. **233**, 96 (1990), https://articles.adsabs.harvard.edu/pdf/1990A%26A...233...96E.
[28] V. Grebenyuk et al. (NUCLEON Collaboration), arXiv:1809.07285.
[29] K. A. Lave et al., Astrophys. J. **770**, 117 (2013).
[30] A. C. Cummings, E. C. Stone, B. C. Heikkila, N. Lal, W. R. Webber, G. Jóhannesson, I. V. Moskalenko, E. Orlando, and T. A. Porter, Astrophys. J. **831**, 18 (2016).
[31] E. Juliusson, Astrophys. J. **191**, 331 (1974).
[32] G. Minagawa, Astrophys. J. **248**, 847 (1981).
[33] J. A. Lezniak and W. R. Webber, Astrophys. J. **223**, 676 (1978).
[34] J. S. Young, P. S. Freier, C. J. Waddington, N. R. Brewster, and R. K. Fickle, Astrophys. J. **246**, 1014 (1981).
[35] J. Esposito et al., Astropart. Phys. **1**, 33 (1992).
[36] O. Adriani et al. (CALET Collaboration), Phys. Rev. Lett. **119**, 181101 (2017).
[37] O. Adriani et al. (CALET Collaboration), Phys. Rev. Lett. **120**, 261102 (2018).
[38] O. Adriani et al. (CALET Collaboration), Phys. Rev. Lett. **122**, 181102 (2019).
[39] S. Torii and P. S. Marrocchesi (CALET Collaboration), Adv. Space Res. **64**, 2531 (2019).
[40] S. Torii (CALET Collaboration), Proc. Sci., ICRC2017 (**2017**) 1092.
[41] Y. Asaoka (CALET Collaboration), Proc. Sci., ICRC2019 (**2019**) 001.
[42] P. S. Marrocchesi, Proc. Sci., ICRC2021 (2021) 010.
[43] P. S. Marrocchesi et al., Nucl. Instrum. Methods Phys. Res., Sect. A **659**, 477 (2011).
[44] Y. Akaike (CALET Collaboration), Proc. Sci., ICRC2015 (**2015**) 613.
[45] G. Bigongiari (CALET Collaboration), Proc. Sci., ICRC2015 (**2015**) 592.
[46] T. Niita, S. Torii, Y. Akaike, Y. Asaoka, K. Kasahara, S. Ozawa, and T. Tamura (CALET Collaboration), Adv. Space Res. **55**, 2500 (2015).
[47] Y. Asaoka et al. (CALET Collaboration), Astropart. Phys. **91**, 1 (2017).
[48] P. Maestro and N. Mori (CALET Collaboration), Proc. Sci., ICRC2017 (**2017**) 208.
[49] K. Kasahara, in Proceedings of the 24th International Cosmic Ray Conference (Rome, Italy 1995), Vol. 1, p. 399, https://ui.adsabs.harvard.edu/abs/1995ICRC....1..399K.

[50] See EPICS webpage http://cosmos.n.kanagawa-u.ac.jp/EPICSHome/.

[51] S. Roesler, R. Engel, and J. Ranft, in *Advanced Monte Carlo for Radiation Physics, Particle Transport Simulation and Applications* (Springer, Berlin, Heidelberg, 2000), pp. 1033–1038, https://link.springer.com/chapter/10.1007/978-3-642-18211-2_166.

[52] J. Allison *et al.*, Nucl. Instrum. Methods Phys. Res., Sect. A **835**, 186 (2016).

[53] See Supplemental Material at http://link.aps.org/supplemental/10.1103/PhysRevLett.128.131103 for supporting figures and the tabulated fluxes, as well as the description of the data analysis procedure and the detailed assessment of systematic uncertainties.

[54] G. D'Agostini, Nucl. Instrum. Methods Phys. Res., Sect. A **362**, 487 (1995).

[55] T. Adye, *Proceedings of the PHYSTAT 2011 Workshop on Statistical Issues Related to Discovery Claims in Search Experiments and Unfolding* (CERN, Geneva, Switzerland, 2011), https://arxiv.org/abs/1105.1160.

[56] R. Brun and R. Rademakers, Nucl. Instrum. Methods Phys. Res., Sect. A **389**, 81 (1997).

[57] D. Maurin, H. P. Dembinski, J. Gonzalez, and I. C. Mariş, and F. Melot, Universe **6**, 102 (2020).

[58] Y. Akaike (CALET Collaboration), J. Phys. Conf. Ser. **1181**, 012042 (2019).